POLITECNICO
MILANO 1863

SCUOLA DI INGEGNERIA INDUSTRIALE
E DELL'INFORMAZIONE

Executive Summary of the Thesis

Selective Volume Illumination Microscopy for Compressed Sensing of time lapse series

Laurea Magistrale in Engineering Physics – Ingegneria Fisica

Author: Marco Tobia Vitali

Advisor: Prof. Andrea Bassi

Co-advisors: Prof. Alessia Candeo, Gianmaria Calisesi Ph.D.

Academic year: 2021-2022

1. Introduction

We built and tested a fluorescence microscope that combines Light Sheet Fluorescence Microscopy with Compressed Sensing for the 4D imaging of live biological samples. Our aim was to achieve temporal resolutions in the order of 20 ms using common and relatively inexpensive optical components.

1.1. Fast sampling of volumes

Fluorescence Microscopy is extensively used in experimental biology because of its high sensitivity and specificity. Moreover, it allows to image live samples that range from single molecules to whole organisms. Standard microscopy techniques (like confocal microscopy) do not offer sufficient temporal resolution to study physiological processes that evolve on the millisecond time scale.
Selective Plane Illumination Microscopy (SPIM), also known as *Light Sheet Fluorescence Microscopy* (LSFM), is widely employed to record 4D images (i.e., volumes throughout time): it offers low photobleaching and high temporal resolution by simultaneously exposing and imaging all the points lying on a plane.
The temporal resolution of conventional SPIM setups is limited by the need to mechanically translate either the sample or the detection objective. Fahrbach et al. [1] solved these problems using tunable optic elements to move the detection focus plane on the scanning illumination sheet. Their microscope had no moving parts and allowed to image 17 planes at 510 frames per second, which corresponded to 30 volume scans per second.
Recently, systems with increasing complexity and costs have achieved high temporal resolutions. For example, the combination of Swept confocally-aligned planar excitation (SCAPE) microscopy with a cooled image intensifier camera (which reached 12719 frames per second for a 640 × 148 pixel active sensor) achieved acquisition speeds beyond 100 volumes/s [2].

1.2. Compressed Sensing

Compressed sensing allows to increase the temporal resolution of 4D scans. Its efficiency in gathering information allows one to reduce the number of measurements needed to collect the most relevant features of an unknown sample [3]. To sample an unknown vector $\boldsymbol{x}$ of dimension N, we can use a measurement matrix $\boldsymbol{\Phi}$ (with M rows and N columns) that translates its in-

formation into quantities $\boldsymbol{y}$ that we can easily record and analyse: $\boldsymbol{y} = \boldsymbol{\Phi} \cdot \boldsymbol{x}$. To find $\boldsymbol{y}$ we need to perform M different measurements as each value $y_m = \boldsymbol{\varphi}_m \cdot \boldsymbol{x}$ is the projection of $\boldsymbol{x}$ on $\boldsymbol{\varphi}_m$, the m-th row of $\boldsymbol{\Phi}$.
With compressed sensing we aim to perform a smaller number of measurements than normally necessary, that is, M is smaller than N and we face an ill posed problem. We can look for $\boldsymbol{x}$ by solving the following *Least square* problem:

$$\underset{\boldsymbol{x}}{\operatorname{argmin}}\Big(\big\|\boldsymbol{y} - \boldsymbol{\Phi} \cdot \boldsymbol{x}\big\|_{l_2}^2 + \tau\mathcal{R}(\boldsymbol{x})\Big). \qquad (1)$$

In the last equation, $\tau\mathcal{R}(\boldsymbol{x})$ is a "regularization" or "penalty" function that we add to promote certain features in the solution. In this way, $\boldsymbol{x}$ will minimize both the loss function and the penalty function with a relative priority given by the parameter τ.
The choice of the measurement matrix $\boldsymbol{\Phi}$ is crucial for a good reconstruction of compressed data: we want to create redundancy in each measurement so that we can skip some of them and still uniformly sample the whole $\boldsymbol{x}$ space. This constraint immediately makes orthogonal basis unsuitable for compressed sensing as removing a base element leaves a degree of freedom of $\boldsymbol{x}$ completely unmeasured.

1.3. Compressed sensing light sheet

To introduce compressive sensing in fluorescence microscopy, we needed to formalize the fluorescent emission from a given point in the sample. Fluorescence intensity is the product between the illumination intensity and the concentration of fluorophores. Let $\boldsymbol{x}_{(i,j)} \in \mathbb{R}^N$ be the unknown fluorescence distribution along the Z-direction for a given (i, j) point in the XY plane. Moreover, let $\boldsymbol{\varphi}_m \in \mathbb{R}^N$ be the z-modulated illumination light pattern that we project during the acquisition of the m-th camera frame.
Each pixel of a CMOS camera integrates all the fluorescent emission generated within the Point Spread Function (PSF) of the detection objective. We worked under the hypothesis that the PSF of our system was confined in the plane parallel to the camera sensor (XY) and elongated along the axial direction (Z). We wanted a detection objective with a depth of field long enough to cover the Z-dimension of our volume of interest.
Under these hypothesis, the intensity $y_{(i,j),m} \in \mathbb{R}$ recorded by the (i, j) camera pixel is given by: $y_{(i,j),m} = \boldsymbol{\varphi}_m \cdot \boldsymbol{x}_{(i,j)}$, where the scalar product formally performs the integration along the Z-axis. If we perform M measurements, $m \in \{1, ..., M\}$, then the raw data set $\boldsymbol{y}$ is the result of the following matrix product: $\boldsymbol{y}_{(i,j)} = \boldsymbol{\Phi} \cdot \boldsymbol{x}_{(i,j)}$.
As each one of the N Z-planes can be illuminated or left dark, the entries of $\boldsymbol{\varphi}_m$ encode these two states with values 1 and 0 respectively.
SPIM is not compatible with compressed sensing because its measurement matrix is the identity matrix (i.e., an orthogonal base). We therefore needed to shape the illumination in a more complex and rich way to be able to take advantage of compressive sensing. While SPIM illuminates one plane at a time, we worked on the volume as a whole, moving to what is called Selective Volume Illumination Microscopy (SVIM).
Calisesi et al. [4] designed a Spatially Modulated Selective Volume Illumination Microscope (smSVIM) that used the modified light sheet setup to implement compressed sensing for the acquisition of a single volume.
The objective of this thesis was to build a variation of this smSVIM microscope and achieve compressive sensing of a time series of volumes. In particular, we wanted to extend the hypothesis of sample regularity to the time dimension and reconstruct each volume taking into account information coming from neighboring time points.

2. Materials and methods

2.1. Optical setup

To shape the illumination of our volume of interest we used Digital Micromirror Devices (DMDs). They are efficient and inexpensive Spatial Light Modulators (SLMs). DMDs feature an array of micrometric mirrors that can be individually tilted to a $\pm 12^\circ$ positions. As a result, light shining on the DMD can be deflected by each mirror along two different paths. On one of these paths we placed the sample so that by tilting each mirror we could decide whether to shine light on the sample or divert it away. In this way, the DMD applied a binary amplitude modulation mask to the illumination beam.
We used two telescopes to conjugate the DMD and samples planes; in this way, we could deliver

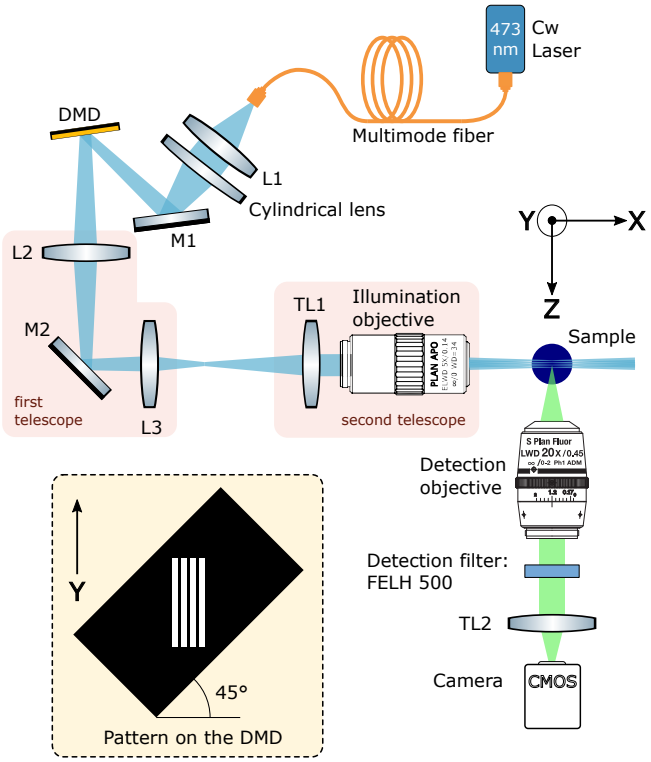

Component	Specification
CW laser	473 nm, 40 mW
MM fiber	200 µm core diameter
L1	$f_1 = 30$ mm
Cyl. lens	$f_{CL} = 300$ mm (y axis)
DMD	Texas Instruments DLP6500, 7.56 µm × 7.56 µm mirrors
L2	$f_2 = 150$ mm
L3	$f_3 = 75$ mm
TL1	$f_{TL1} = 180$ mm
Ill. obj.	$f_{I.O.} = 40$ mm, NA = 0.14
Det. obj.	Nikon 20×, NA = 0.45
Det. filter	FELH 500 nm
TL2	Nikon, $f_{TL2} = 200$ mm
Camera	Hamamatsu ORCA-Flash4.0 V2, 6.5 µm × 6.5 µm pixels, 100 fps for 2048×2048 px active sensor

Figure 1: **smSVIM microscope configuration.** This scheme shows the complete setup of the microscope. The main specifications of each part are reported in Table on the right. In the bottom left portion of this figure we see an example of how DMD patterns must be designed to create modulated illumination along the z-axis (as the four lines are parallel to the Y-axis).

to the sample the pattern created by the bright and dark pixels of the DMD (Fig. 1). With a calibration glass we experimentally determined that the detection magnification was 19.2 (with a nominal 20× detection objective) and that the illumination magnification from the DMD to the sample was $M_{exp} = 8.94$.

We introduced a cylindrical lens to focus the laser beam in one direction to address the power loss caused by the shape difference between the circular laser beam and the rectangular DMD active region. The long focal length of this lens partially justifies the absence of a second cylindrical lens that recollimates the beam (like in a "4f" telescope). Indeed, after testing the system with a proper cylindrical telescope, we found out that a single lens with a long focal length worked just as well: after the DMD, the divergence of the beam due to the single lens did not produce visible artifacts.

Typical Light Sheet microscopes use coherent laser light to illuminate the sample. Indeed, laser sources are well suited for real time imaging because of their high radiance (i.e., energy density): even with short exposure times, they can provide sufficient fluorophore excitation and acceptable signal to noise ratios. However, laser light creates striping artifacts and speckle patterns. Striping artifacts (i.e., shadows) are created by dense media within the sample as the highly directional laser light fails to recover after an obstacle.

While Huisken et al. [5] tackled these problems by using multi-directional illumination, Calisesi et al. [4] opted for an incoherent light source (an LED). In our case, to take advantage of the high intensity of a laser source while avoiding the artifacts entailed by coherent illumination, we chose to use a continuous wave diode laser coupled to a multimode optical fibre. The large core of this fibre (200 µm) allowed to achieve very good coupling efficiency and, more importantly, it greatly deteriorated the laser light coherence.

The samples were first enclosed in 2% agarose and then lowered in a quartz cuvette filled with distilled water. The glass of the cuvette was

1.30 mm thick and the water was confined in a square of $(10.00\,\text{mm})^2$.
We strove to efficiently upload patterns on the DMD. We created patterns at the beginning of each measurement to avoid using a static pre-made collection (which could not be modified between experiments). The whole microscope is managed through *ScopeFoundry*, a Python based instrument control application that manages both data acquisition and visualization [6]. ScopeFoundry allows us to interact with the hardware and to execute custom designed measurements (`https://github.com/marccv/smSVIM`).

2.2. Increasing the detection depth of focus

To use a SVIM microscope we needed a sufficiently large detection depth of focus to uniformly integrate the emitted fluorescence along the Z direction.
Tomer et al. [7] devised a SPherical-aberration-assisted Extended Depth-of-field light sheet microscope (SPED-LS) where sample and detection objective were kept stationary while the light sheet was scanned within the detection depth of focus. The depth of focus was purposefully extended in the axial direction (i.e., Z-axis) by introducing spherical aberrations in the detection path. For this purpose, a layer of medium with refractive index higher than air (for objectives that are aberration corrected in air) was inserted between the sample and the detection objective. The PSF axial FWHM increased with the layer's refractive index and thickness.
We found that the depth of focus of our setup was sufficiently large to uniformly image our volume of interest (with a Z extent of 76.5 µm). The elongation of the PSF was caused by intrinsic aberrations in the detection arm: we used a detection objective designed to work in air (20× Nikon, NA = 0.45) to image a sample that was placed behind layers of glass and water. Over the nominal air working distance of the objective (8.2 mm) we find circa 4 mm of water and a 1.30 mm slab of glass.
We directly measured the detection PSF by illuminating the whole volume of interest (76.5 µm in Z) and translating sub-diffraction beads (160 nm in diameter) by steps of 2 µm along the

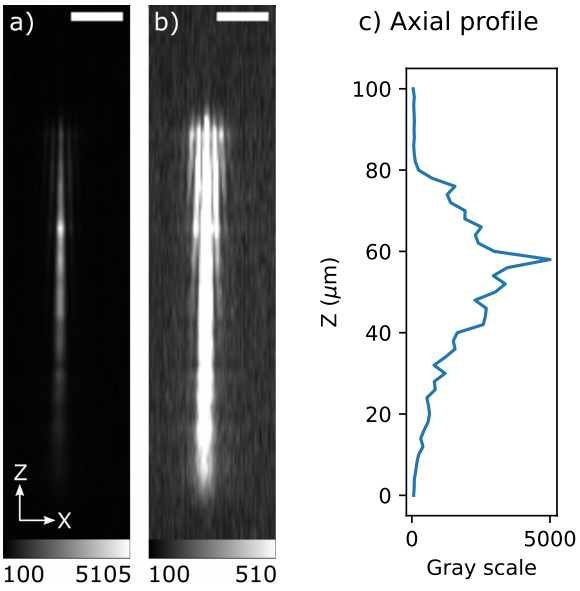

Figure 2: **Detection objective PSF. a, b)** XZ planes that contain the PSF brightest point shown with two different contrasts. The scale bars are 10 µm long. **c)** PSF Z-profile in the XY coordinate of its brightest point.

Z-axis. We recorded 51 frames to cover a span of 100 µm in the Z direction. In this way, we could follow a single bead as it passed through different portions of the detection PSF (Fig. 2). The aberrated air detection offers an elongated PSF that more or less spans across the z region of interest (ROI). The PSF is asymmetric along the Z axis and exhibits rings only on one side.

2.3. Measurement matrix

We adopted measurement matrices built with *Hadamard* patterns because they have been found to work well with compressed sensing [3]. A Hadamard matrix $\boldsymbol{H}_N$, is a $N \times N$ matrix with entries $+1$ and -1 that satisfies $\boldsymbol{H}_N \boldsymbol{H}_N^T = \boldsymbol{H}_N^T \boldsymbol{H}_N = N\boldsymbol{I}_{\boldsymbol{N}}$, where $\boldsymbol{I}_{\boldsymbol{N}}$ is the N dimensional identity matrix. We can recursively build Hadamard matrices by defining $H_1 = 1$ and, for $k \in \mathbb{N}^+$,

$$H_{2^k} = \begin{bmatrix} H_{2^{k-1}} & H_{2^{k-1}} \\ H_{2^{k-1}} & -H_{2^{k-1}} \end{bmatrix}. \tag{2}$$

Figure 3 shows the *Walsh* version of H_{16} where rows were ordered by increasing spatial frequency. While the first row of these symmetric matrices has all values set to 1, the remaining rows have half of the entries equal to 1's and

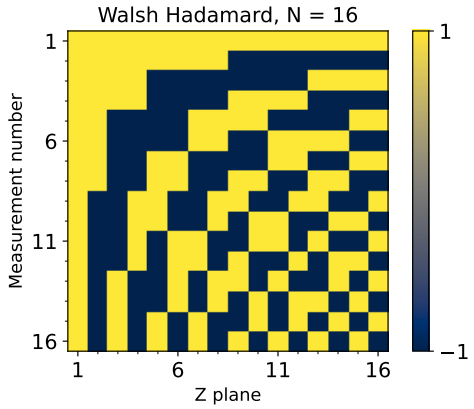

Figure 3: **Walsh Hadamard matrix.**

half equal to -1's (fill factor $1/2$). This property survives even if we *scramble* H_N by randomly permuting its rows and columns.
Hadamard pattern are well suited for DMDs as they have binary entries. However, DMDs can only show 0's and 1's. This leaves us two choices: we can either replace all the -1 entries with a 0 and work with a positive measurement matrix $\boldsymbol{\Phi}$, or express each row of $\boldsymbol{H}$ (that is, each measurement) as the subtraction of two positive patterns. We called the first method *Single Frame* and the second one *Double Frame*. Here is an example of the second method applied to the m-th row $\boldsymbol{\varphi}_m = [1, -1]$ of a measurement matrix with $N = 2$:

$$\begin{aligned} y_m = y_m^+ - y_m^- = [1,0]\cdot\boldsymbol{x} - [0,1]\cdot\boldsymbol{x} = \\ = [1,-1]\cdot\boldsymbol{x} = \boldsymbol{\varphi}_m\cdot\boldsymbol{x}, \end{aligned} \tag{3}$$

where y_m^+ and y_m^- are the physical values that we record in two subsequent camera frames.
The significant advantage of a *Double Frame* acquisition lies in its intrinsic and robust background subtraction. Moreover, the subtraction of two frames leads to a signal to noise ratio $\sqrt{2}$ times higher. The great cost we need to pay for this features, is the doubling of the number of frames needed to reconstruct a single volume.
We also employed an ex-post method to reconstruct negative values in a *Single Frame* data set. This method independently worked on XY pixels by subtracting from the raw data $\boldsymbol{y}$ the average of the measures y_m that were acquired with high spatial frequency patterns. For Walsh patterns, we performed this operation by subtracting the average of the values y_m for $m \geqslant l$. We empirically set $l = 7$ when $N = 16$.
The matrices used for the inverse problem were:

- The Walsh matrix with ± 1s for *Double Frame* data sets and *Single Frame* data sets where negative values were reconstructed.
- The Walsh matrix matrix with negative values set to zero for the *Single Frame* data set.

2.4. Compressed Sensing in 4D imaging

Time lapse measurements can really take advantage of Compressed sensing as they can use temporal regularization to reconstruct volumes that otherwise are too undersampled to be independently used.
If the camera sensor has n_V rows and n_H columns, $\boldsymbol{x}_{(i,j)} \in \mathbb{R}^N$ with $i = 1, \ldots, n_V$ and $j = 1, \ldots, n_H$ are the unknown Z fluorescence distributions in front of every (i, j) camera pixel in a given time point.
To handle the complete time series, let us define $\boldsymbol{x}^t \in \mathbb{R}^{(N\cdot n_V\cdot n_H)}$ as the column vector built by vertically stacking all the $\boldsymbol{x}_{(i,j)}$ of a given time point $t = 1, \ldots, T$ (where T is the total number of volumetric time points). Moreover, let us define a column vector $\hat{\boldsymbol{x}} \in \mathbb{R}^{(N\cdot n_V\cdot n_H\cdot T)}$ built by vertically stacking the different time points $\boldsymbol{x}^t$ $(\forall\ t = 1, \ldots, T)$.
It is also useful to arrange the dynamic sample $\hat{\boldsymbol{x}}$ in a *Casorati* matrix $\mathrm{C}(\hat{\boldsymbol{x}})$. By definition, the columns of this matrix are the different time points:

$$\mathrm{C}(\hat{\boldsymbol{x}}) \equiv [\boldsymbol{x}^1,\ \boldsymbol{x}^2, \ldots,\ \boldsymbol{x}^T] \in \mathbb{R}^{(N\cdot n_V\cdot n_H)\ \times\ T}. \tag{4}$$

The measurement matrix $\hat{\boldsymbol{\Phi}}$ that we apply to $\hat{\boldsymbol{x}}$ is a block diagonal matrix built by repeating $n_V \cdot n_H$ times the measurement matrices $\boldsymbol{\Phi}_t \in \mathbb{R}^{M\times N}$ of each time point t. This way, the direct problem is defined for the whole time series but each $\boldsymbol{x}_{(i,j)} \in \mathbb{R}^N$ is still independently measured. The complete measured data $\hat{\boldsymbol{y}} = \hat{\boldsymbol{\Phi}}\cdot\hat{\boldsymbol{x}}$ is structured in the same way as $\hat{\boldsymbol{x}}$.
While Calisesi et al. [4] exclusively exploited spatial redundancies to reconstruct an undersampled volume, Tourais et al. [8] extended the hypothesis of sample regularity to the temporal dimension and were able to reconstruct compressed magnetic resonance dynamic images. In particular they used the alternating direction method of multipliers (ADMM) to solve the following problem:

$$\underset{\hat{\boldsymbol{x}}}{\operatorname{argmin}}\Big(\left\|\hat{\boldsymbol{y}}-\hat{\boldsymbol{\Phi}}\cdot\hat{\boldsymbol{x}}\right\|_{l_2}^2+ \\ +\alpha\left\|\mathrm{C}(\hat{\boldsymbol{x}})\right\|_*+\beta\left\|\mathrm{TV}(\hat{\boldsymbol{x}})\right\|_{l_1}\Big). \tag{5}$$

The two regularization terms respectively promote regularity in time and in space (with α and β as regularization parameters).
The regularization over time was built on the hypothesis that time points are mutually correlated because they follow a sufficiently slow movement of a given structure. Formally, this redundancy generates a *Low rank Casorati* matrix of the sample. We enforced this constraint by minimizing the sum of the singular values (that is, the nuclear norm $\| \bullet \|_*$) of $\mathrm{C}(\hat{\boldsymbol{x}})$.
On the other hand, spatial regularization is introduced by minimizing the anisotropic *Total Variation* of the sample: $\|\mathrm{TV}(\hat{\boldsymbol{x}})\|_{l_1} \equiv \|\nabla_x\hat{\boldsymbol{x}}\|_{l_1}+\|\nabla_y\hat{\boldsymbol{x}}\|_{l_1}+\|\nabla_z\hat{\boldsymbol{x}}\|_{l_1}$.

3. Results

We proceeded to test the system on the zebrafish beating heart. The samples were prepared by the Department of Bioscience of the University of Milano following standard procedures. Decorionated specimen were delivered to us two days post fertilization.
We worked with zebrafish fluorescenct in the vasculature and blood cells. They were kept in 0.003% 1-phenyl-2-thiourea (PTU) to inhibit the melanization of tissues.
To reduce the movement of the fish during data set acquisition, we anesthetized samples by placing them in 0.016% tricaine (Ethyl 3-aminobenzoate methanesulfonate salt) and we restrained them in low melting point 2% agarose gel. The liquid gel with the sample was drawn in a capillary so that after its solidification we could extrude an agarose cylinder. During acquisitions, we lowered the sample in the cuvette which was filled with fish water (Instant Ocean, 0.1% Methylene Blue).

3.1. Acquisition of complete data sets

We decided to test the system by acquiring complete data sets. In this way, we could retrospectively apply different types of data compression and optimize the reconstruction algorithms. We needed to verify that the system was fast enough to produce temporally correlated time points: if the sample moves too fast for our system, the hypothesis of temporal regularity will not stand. Moreover, we wanted to investigate if introducing Low Rank temporal regularization offered substantial advantages over spatial regularization of individual time points.
Table 1 reports the details of the experiments carried out without direct use of compressed sensing. We used scrambled Hadamard matrices with dimension $N = 16$; patterns were displayed on the DMD with a binning equal to 4. The voxel Z dimension was $(4 \cdot \sqrt{2} \cdot 7.56\,\mu\mathrm{m}) \,/\, M_{exp} = 4.78\,\mu\mathrm{m}$, where 4 is the DMD binning, $\sqrt{2} \cdot 7.56\,\mu\mathrm{m}$ is the diagonal length of a DMD pixel and $M_{exp} = 8.94$ is the experimental illumination magnification.

Parameters	**Description**	
Markers	KDRL + GATA	
Det. Obj.	Nikon 20×, NA = 0.45	
Voxel (X,Y,Z)	$(0.339, 0.339, 4.78)\mu$m	
Volume dim.	X: 256 px → 86.8 µm	
	Y: 2048 px → 694 µm	
	Z: 16 px → 76.5 µm	
Laser power	40 mW	
Exp. time	1.208 ms	
Read out time	1.388 ms	
Frame rate	386.3 Hz	
Measurements	$N = M = 16$ (no CS)	
	Single Frame	**Double Frame**
Frames/pattern	1	2
Frames/volume	16	32
Time/volume	41.41 ms	82.82 ms
Pattern type	Scrambled Hadamard with different permutation for each time point	

Table 1: **Experimental details for non-compressed data sets.**

3.2. Inversion tests

To test the algorithms and the effect of Low Rank regularization we inverted the complete data sets in three ways:

- We used all the acquired frames ($M = N = 16$) to obtain a non-compressed reconstruction. In this case, we did not apply Low rank or Total Variation regularization ($\alpha = 0$ and $\beta = 0$ in Eq. 5)

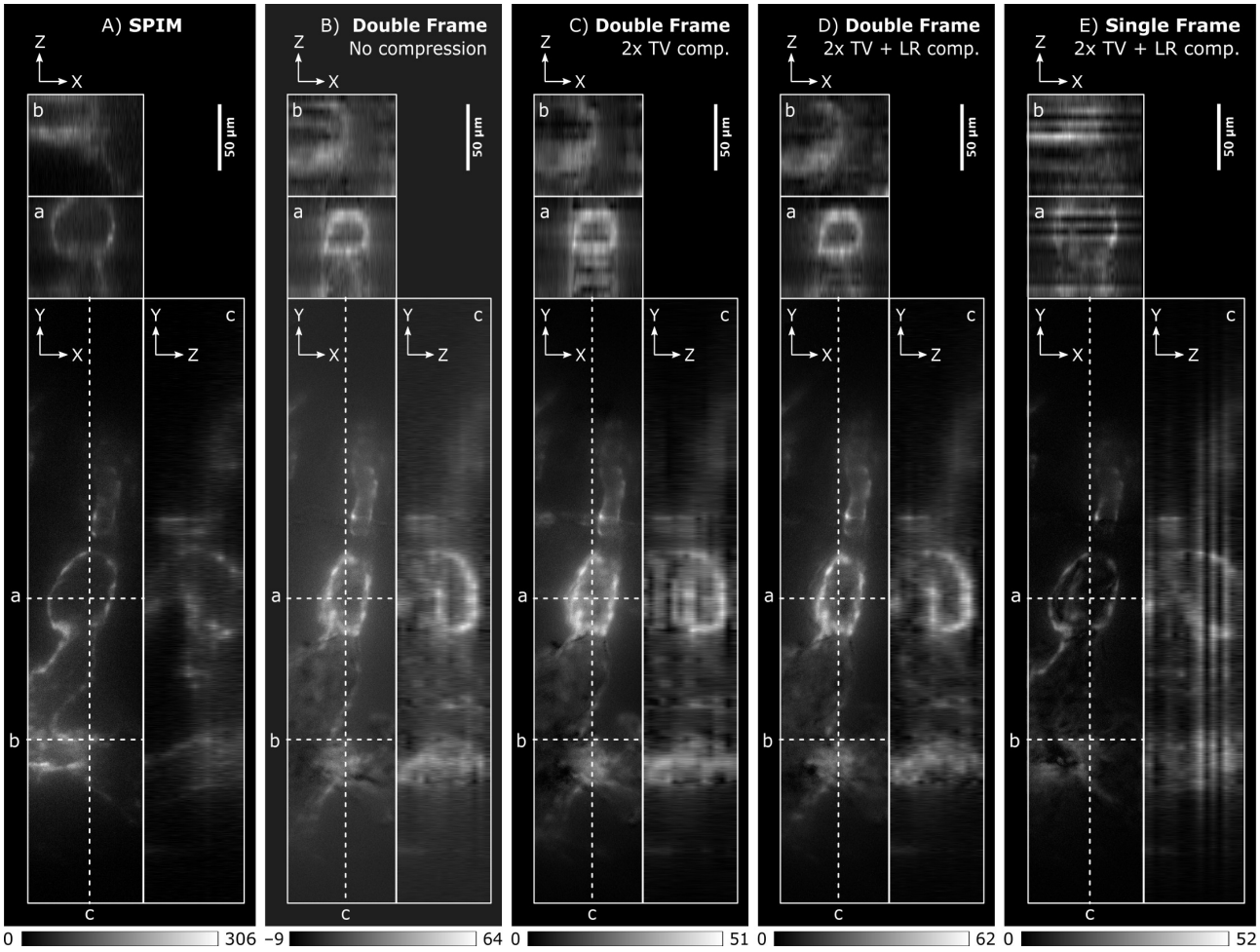

Figure 4: **DMD SPIM and smSVIM reconstructions** Panel A shows the reference light sheet reconstruction of the zebrafish heart. Panel C shows the inversion of a retrospectively down-sampled *Double Frame* data set (2× compression) regularized with Total Variation (TV). Panel D shoes how the TV reconstruction is improved when also applying Low Rank temporal regularization. The *Single Frame* inversion of panel E doubled the volume sampling frequency but featured strong artifacts and has lower signal to noise ratio.

- We performed an ex-post 2× compression and applied only Total Variation (TV, i.e. spatial) regularization. We discarded half of the acquired frames to bring $M = N/2 = 8$ and we used $\alpha \neq 0$ and $\beta = 0$ in Eq. 5.
- We performed an ex-post 2× compression and applied both spatial and temporal regularization (Low Rank). We discarded half of the acquired frames to bring $M = N/2 = 8$ and we used $\alpha \neq 0$ and $\beta \neq 0$ in Eq. 5.

Figure 4.A shows a reference volume reconstruction built using light sheet sectioning. With the DMD we produced a 4.78 µm thick light sheet and we moved it along the Z axis.

Figure 4 shows orthogonal sections of a *Double Frame* time point inverted with the three different methods. Fig. 4.C indicates that TV spatial regularization of independent volumes struggled to yield clean images and that we needed time regularization to reconstruct the compressed time lapse (Fig. 4.D). Using compression, $M = 16/CS_{ratio}$ becomes too small to independently reconstruct each volume (i.e., with $\alpha = 0$ in Eq. 5).

At this point we tested if we could improve the reconstruction by using the *Single Frame* scheme. Figure 4.E shows how we obtained crispier details than in the *Double Frame* acquisition. However, they also had lower signal to noise ratio and strong planar artifacts (in different XY planes across different time points).

4. Conclusions

We built a fluorescence microscope to perform 4D imaging of dynamic samples with a time resolution of circa 40 ms. Starting from Light Sheet Fluorescence Microscopy and Spatially Modulated Selective Volume Illumination Microscopy, we worked to implement Compresses Sensing and increase the volume sampling rate.
The system was optimized and we were able to reach frame rates previously not accessible in our laboratory. In particular, we payed close attention to hardware management: we used Python to control the DMD and the camera during experiments. The resulting acquisition time of a single volume was compatible with Low Rank compressed sensing: even without compression, the temporal resolution was sufficient to smoothly follow events that evolved on the millisecond time scale.
We experimented with different methodologies for the inversion of complete and retrospectively compressed data sets. We found that temporal regularization (with Low Rank) was pivotal for the reconstruction of time series that have few measurement for each volume. In the future, we expect to achieve better results with data sets that were compressed during data acquisition.

References

[1] F. O. Fahrbach, F. F. Voigt, B. Schmid, F. Helmchen, and J. Huisken, "Rapid 3d light-sheet microscopy with a tunable lens," *Opt. Express*, vol. 21, no. 18, pp. 21 010–21 026, Sep 2013. [Online]. Available: https://opg.optica.org/oe/abstract.cfm?URI=oe-21-18-21010

[2] V. Voleti, K. B. Patel, W. Li, C. Perez Campos, S. Bharadwaj, H. Yu, C. Ford, M. J. Casper, R. W. Yan, W. Liang, C. Wen, K. D. Kimura, K. L. Targoff, and E. M. C. Hillman, "Real-time volumetric microscopy of in vivo dynamics and large-scale samples with scape 2.0," *Nature Methods*, vol. 16, no. 10, pp. 1054–1062, 2019. [Online]. Available: https://doi.org/10.1038/s41592-019-0579-4

[3] G. Calisesi, A. Ghezzi, D. Ancora, C. D'Andrea, G. Valentini, A. Farina, and A. Bassi, "Compressed sensing in fluorescence microscopy," *Progress in Biophysics and Molecular Biology*, vol. 168, pp. 66–80, 2022. [Online]. Available: https://www.sciencedirect.com/science/article/pii/S007961072100064X

[4] G. Calisesi, M. Castriotta, A. Candeo, A. Pistocchi, C. D'Andrea, G. Valentini, A. Farina, and A. Bassi, "Spatially modulated illumination allows for light sheet fluorescence microscopy with an incoherent source and compressive sensing," *Biomed. Opt. Express*, vol. 10, no. 11, pp. 5776–5788, Nov 2019. [Online]. Available: http://opg.optica.org/boe/abstract.cfm?URI=boe-10-11-5776

[5] J. Huisken and D. Y. R. Stainier, "Even fluorescence excitation by multidirectional selective plane illumination microscopy (mspim)," *Opt. Lett.*, vol. 32, no. 17, pp. 2608–2610, Sep 2007. [Online]. Available: https://opg.optica.org/ol/abstract.cfm?URI=ol-32-17-2608

[6] [Online]. Available: http://www.scopefoundry.org

[7] R. Tomer, M. Lovett-Barron, I. Kauvar, A. Andalman, V. M. Burns, S. Sankaran, L. Grosenick, M. Broxton, S. Yang, and K. Deisseroth, "Sped light sheet microscopy: Fast mapping of biological system structure and function," *Cell*, vol. 163, no. 7, pp. 1796–1806, 2022/10/06 2015. [Online]. Available: https://doi.org/10.1016/j.cell.2015.11.061

[8] J. Tourais, C. M. Scannell, T. Schneider, E. Alskaf, R. Crawley, F. Bosio, J. Sanchez-Gonzalez, M. Doneva, C. Schülke, J. Meineke, J. Keupp, J. Smink, M. Breeuwer, A. Chiribiri, M. Henningsson, and T. Correia, "High-resolution free-breathing quantitative first-pass perfusion cardiac mr using dual-echo dixon with spatio-temporal acceleration," *Frontiers in Cardiovascular Medicine*, vol. 9, 2022. [Online]. Available: https://www.frontiersin.org/articles/10.3389/fcvm.2022.884221